INVESTIGATION ON PROPELLER SLIPSTREAM BY USING AN UNSTRUCTURED RANS SOLVER BASED ON OVERLAPPING GRIDS

X. Q. Gong*

School of Aeronautics
Northwestern Polytechnical University
Xi'an, China

M. S. Ma **J. Zhang** **J. Tang**

Computational Aerodynamics Institute
China Aerodynamics Research and Development Center
Mianyang, China

ABSTRACT

Based on unstructured hybrid grid and dynamic overlapping grid technique, numerical simulations of Unsteady Reynolds Averaged Navier-Stokes equations were performed and investigation on isolated propeller aerodynamic characteristics and effects of propeller slipstream on turboprops were undertaken. The computational grid consisted of rotational subzone of propeller and stationary major-zone of aircraft, and walls criterion was used in the automatic hole-cutting procedure. Distance weight interpolation and tri-linear interpolation were developed to transfer information between the rotational and stationary subzones. The boundaries of overlapping grids were optimized for fixed axis rotation. The governing equations were solved by dual-time method and Lower Upper-Symmetric Gauss-Seidel method. The method and grid technique were verified by isolated propeller configuration and the computational results were in well agreement with the experimental data. The grid independence was studied to establish the numerical results. Finally, the flow around a turboprop case was simulated and the influence of propeller slipstream was presented by analyzing the surface pressure contours, profile pressure distribution, vorticity contours and profile streamline. It's indicated that the slipstream accelerates and rotates the free stream flow, changing the local angle of attack, enhancing the downwash effects, affecting the pressure distribution on wing and horizontal tail, as well as increasing the drag coefficient, pitching moment coefficient and the slope of lift coefficient.

Keywords: Unstructured hybrid grid, Overlapping grid, Propeller slipstream, Unsteady flow simulation.

1. INTRODUCTION

Compared to turbojet and high bypass turbofan, turboprop has such advantages as higher propulsive efficiency, longer cruise time, lower fuel consumption and less pollution, and is widely used in modern aircraft. Since propeller slipstream is very complex, it has a significant impact on the aerodynamic characteristics of aircraft. Accurate prediction and analysis of the slipstream effect and mutual aerodynamic interaction between the propeller and aircraft have become an important subject in the field of fluid mechanics.

In the past few decades, with the development of computational fluid dynamics (CFD), numerical simulation methods of propeller slipstream were developed from the lifting-line theory [1], lifting-surface theory [2] to actuator disk model [3, 4]. Based on structured/unstructured grid, unsteady numerical simulations of propeller slipstream were carried out on the unsteady Euler/Navier-Stokes equations by using dynamic patched grid, slipping grid and overlapping grid techniques. With the application of unstructured grid, Namu [5] numerically simulated the mutual interaction between propeller and fuselage by using Euler equations. Stuermer [6] computed the unsteady flow field of single propeller and the propeller-straight wing interaction with DLR-TAU code. Roosenboom [7] validated the accuracy of CFD methods and codes by Particle Image Velocimetry (PIV) experiments in industrial wind tunnels through the section instantaneous velocity contours and vorticity contours. Xu He-yong [8] studied the single-slip slipstream around propeller airplane by using

* Corresponding author (gxq19842002@163.com.cn)

DOI : 10.1017/jmech.2017.50
Copyright © 2017 The Society of Theoretical and Applied Mechanics
https://doi.org/10.1017/jmech.2017.50 Published online by Cambridge University Press

3-D Euler equations based on unstructured overlapping grids.

Unstructured hybrid grid has no topological structure and is more adaptable to complex configuration, and it's easy to locally refine surface and space grids. Anisotropic triangular grid is able to simulate suction peak at the leading edge well while saving number of grid cells. The overlapping grid method is originally introduced to deal with complicated configuration with structured grids and is quite powerful for dealing with moving bodies, which is suitable for complex configurations and large displacement problems. In this paper, the overlapping grid is used to interpolate the flow variables between the rotational grid and stationary grid. The slipstream of single propeller and turboprop are simulated by solving 3-D Navier-Stokes equations based on anisotropic unstructured hybrid grid. Meanwhile the dynamic overlapping grid technique and parallel hole-cutting technique are developed. The one-equation Spalart-Allmaras (SA) turbulence model [9] is implemented and the full turbulence assumption is used. The governing equations are solved by the dual-time method [10]. The sub-iterations of each physical time step are calculated by using Lower Upper-Symmetric Gauss-Seidel (LU-SGS) [11]. Multi-grid [12], large-scale parallel computing and local time stepping are used to accelerate convergence and improve efficiency.

The purpose of this paper is to study the effects of propeller slipstream by using an unstructured RANS solver based on overlapping grids. The isolated propeller aerodynamic characteristics are compared with experimental data to validate the results of the unsteady computations, and propeller slipstream is researched. Grid independent study is carried out to verify the effects of slipstream on aircraft. Finally, the effects of slipstream on aircraft are analyzed. The remainder of this paper is structured as follows: The governing equations, time-stepping and overlapping grid technique are described in Section 2. The isolated-propeller dynamic characteristics, propeller slipstream and effect on aircraft are presented in Section 3. Concluding remarks are given in Section 4.

2. NUMERICAL METHOD

The computations here were conducted by using the China Aerodynamics Research & Development Center (CARDC) MFlow-code [13-14], which is an unstructured finite volume cell-center CFD solver and has participated in the 5th and 6th CFD drag prediction workshop [15-16]. Second-order accuracy in space is achieved by linear reconstruction in cells. The vertex-based Gauss method is adopted for gradient computations, to simultaneously fulfill accuracy and robustness. Roe scheme [17] is used for inviscid flux computations.

2.1 Governing Equations

The unsteady Navier-Stokes equations are discretized by a cell centered finite-volume method. The integral form of unsteady Navier-Stokes equations for a bounded domain V with a boundary $\partial\Omega$ can be expressed as:

$$\frac{\partial}{\partial t}\iiint_V Q dV + \oiint_{\partial\Omega}\left(H(Q)\cdot\hat{n} - Q\overrightarrow{v_g}\cdot\hat{n}\right)dS = \oiint_{\partial\Omega} H_v(Q)\cdot\hat{n}dS \tag{1}$$

Where $Q = [\rho \quad \rho u \quad \rho v \quad \rho w \quad \rho E]^{\mathrm{T}}$ is the conservative state vector, $\overrightarrow{v_g}$ is the wall velocity and $H(Q)$ is the inviscid flux vector, $H_v(Q)$ is the viscous flux vector. Here, ρ, (u, v, w) and E denote the density, velocity of three directions, and specific total energy of the fluid. $\bar{n}$ is the outward pointing normal unit vector of boundary. The inviscid flux is replaced by a numerical Riemann flux function Roe schemes [17], and the viscous flux is discretized with central difference scheme. The Venkatakrishnan limiter [18] is used to restrict oscillation.

2.2 Time-Stepping

A dual time-stepping is adopted to advance the time-accuracy solution in time. The Lower Upper-Symmetric Gauss-Seidel (LU-SGS) is used to solve Eq. (1), and the sub-iteration of each physical time step is also calculated by using LU-SGS. The forward and backward sweep forms are given in Eqs. (2)-(3), where $\phi = 0.5$, and τ, V^n, v_{nk}, $\lambda_{\max}$, n, N denote the pseudo time, the volume of grid cell, the surface velocity of grid cell, spectral radius, iteration step, surface number of grid cell, respectively.

$$\left(\frac{V_i^{n+1}}{\Delta\tau} + \frac{(1+\phi)V_i^{n+1}}{\Delta t} + \frac{1}{2}\sum_{k=1}^{N}(\lambda_{\max} - v_{nk})S_k\right)\delta Q_i^* = -RHS(Q_i^m) - \frac{1}{2}\sum_{k=1}^{N}\left[\left(H(Q_j^m + \delta Q_j^*) - H(Q_j^m)\right) - \lambda_{\max}\delta Q_j^*\right]S_k \tag{2}$$

$$\delta Q_i^{m+1} = \delta Q_i^* - \frac{1}{2}\left(\frac{V_i^{n+1}}{\Delta\tau} + \frac{(1+\phi)V_i^{n+1}}{\Delta t} + \frac{1}{2}\sum_{k=1}^{N}(\lambda_{\max} - v_{nk})S_k\right)^{-1}\cdot\sum_{k=1}^{N}\left[\left(H(Q_j^m + \delta Q_j^{m+1}) - H(Q_j^m)\right) - \lambda_{\max}\delta Q_j^{m+1}\right]S_k \tag{3}$$

Where,

$$RHS(Q_i^m) = -\frac{(1+\phi)Q_i^n V^n + \phi(Q_i^n V^n - Q_i^{n-1}V^{n-1})}{\Delta t} + \frac{(1+\phi)Q_i^m V^{n+1}}{\Delta t} + \sum_{k=1}^{N} H_k\cdot\bar{n}_k S_k - \sum_{k=1}^{N} H_{vk}(Q^m)\cdot\bar{n}_k S_k \tag{4}$$

https://doi.org/10.1017/jmech.2017.50 Published online by Cambridge University Press

Table 1 Flow parameters of CFD simulation.

Mach number	Pressure (Pa)	Temperature (K)	Speed of sound (m/s)	Advance ratio	Unit Reynolds number	Model scale	Angle of attack (°)
0.147	101325	288.15	340.3	0.716	3.4e+06	1:1	0
0.206	101325	288.15	340.3	1.004	4.8e+06	1:1	0
0.264	101325	288.15	340.3	1.292	6.2e+06	1:1	0
0.294	101325	288.15	340.3	1.432	6.8e+06	1:1	0
0.323	101325	288.15	340.3	1.58	7.5e+06	1:1	0

2.3 Overlapping Grid Hole-Cutting Technique and Interpolation Method

For overlapping grid hole-cutting technique, determination of the hole boundary needs to be fully automated and of high efficiency and robustness. In this paper, the solid surface intersection criterion is selected as the boundary determination method. After determination of the hole boundary, the donor cells in other subzones are found for all interpolated cells. The Alternating Digital Tree method [19] is built for each zone by using the coordinates of the bounding box for a cell, which is a point in six-dimensional space.

Different interpolation methods are used for different types of unstructured grid cells. The tetrahedral and triangular prism cells are interpolated by trilinear interpolation, the pyramid cells use the distance weight and arithmetic average to get the final physical quantities.

$$var = \frac{1}{n}\sum_{i=1}^{n} var_i = \frac{1}{n}\sum_{i=1}^{n}\left(\sum_{j=1}^{k}\frac{1}{r_j}var_j \Big/ \sum_{j=1}^{k}\frac{1}{r_j}\right)_i \tag{5}$$

Where n represents the number of subzones that overlap with the hole boundary cell, and k represents the total number of vertices of the grids in the subzone corresponding to the hole boundary cell, r_j represents the distance between two grid cell centers. In order to ensure the interpolation accuracy of overlapping grid, the grid size in the overlapping interpolation regions should be matched with each other.

2.4 Grid Generation

The computational grid is unstructured hybrid grid, including triangular prism, pyramid, and tetrahedral grid. The triangular prism grid and tetrahedron grid are used to simulate the boundary layer and the isotropic region of the spatial flowfield, respectively, and the pyramid grid is used to transition the triangular prism and the tetrahedron. In order to save the number of grid cells and accurately capture the leading edge suction peak, grids on the front and rear edges of the surface are anisotropic triangular mesh, and the aspect ratio of the surface triangular mesh is controlled below 100. The solid wall of the rotating subzone and the major-zone cannot intersect, and the gap between them must be small. The gap between the rear end of the rotating propeller hub and the front end of the aircraft engine is only 3 mm. In order to ensure the interpolation accuracy, the overlapping region of the two overlapping zones has at least three or four rows of meshes, and the grid size of the overlapping area is almost the same. In order to capture the tip vortex and the slipstream behind the blade, an isotropic tetrahedral mesh is used to refine the grid behind the propeller, and the refined region extends to the tail of the fuselage.

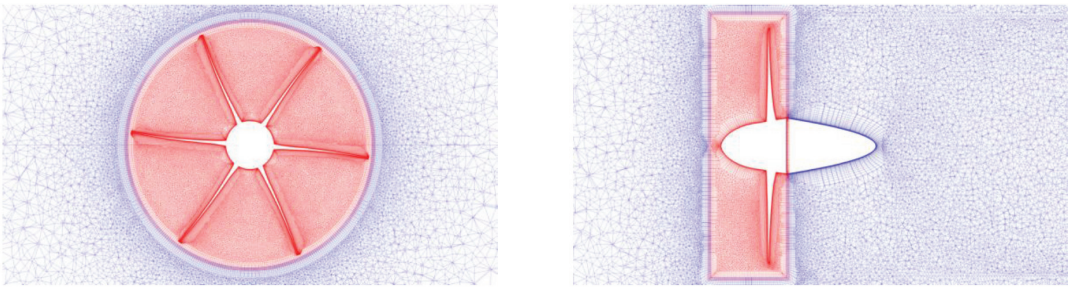
3. RESULTS AND DISCUSSION

3.1 Isolated-Propeller Dynamic Characteristics and Propeller Slipstream Development

The aerodynamic characteristics of a six-bladed propeller at different speeds are numerically simulated. The propeller diameter is 4.1 meters. The propeller rotates with a speed of 1020 rpm and counterclockwise when looking from the front. Experiments are performed in the 8m × 6m Low Speed Wind Tunnel facility of CARDC. The model scale is 1:6 and six-component balance is used to measure the forces and moments of propellers. The test air speed is 35m/s. The test temperature and pressure are 285 K and 95461 Pa, respectively. Table 1 gives the flow parameters of CFD simulation. All the computations are performed on CARDC' computer cluster, whose speed is up to 15.9 trillion floating-point operations per second. The computational domain is decomposed into two overlapping zones, as shown in Fig. 1. The CAD geometry has a small 1mm-gap between hub and fairing. Care is taken to ensure at least four cells make up this and all of the other overlapping regions in each of the two zones. The subzone containing propeller and hub has 10.18 million cells, including tetrahedron, pyramid, and triangular prism, which are 4.6 million, 0.08 million, and 5.5 million respectively. The subzone is cylindrical with the radius of 4.34 meters and height of 1.32 meters. The major-zone containing the fairing is 8 million, of which tetrahedral, pyramid and triangular prism are 7.03 million, 0.02 million and 0.95 million respectively. The major-zone is cylindrical with the radius of 800 meters and height of 800 meters.

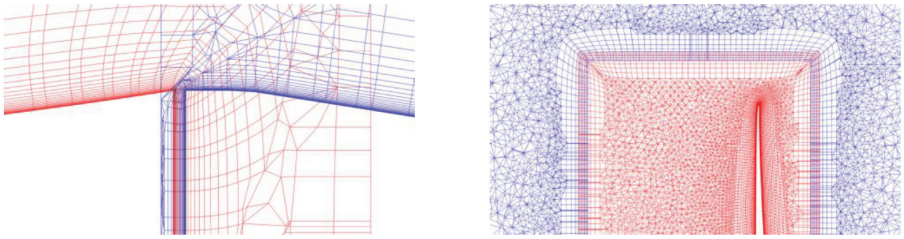
Figures 1(a) and (b) show the X-section and Y-section of propeller overlapping grid. Red mesh represents the subzone of propeller, and blue mesh represents the major-zone. The meshes in the interpolated boundary of the two zones and the meshes behind the propeller are refined, and the extrapolated mesh is generated on the

https://doi.org/10.1017/jmech.2017.50 Published online by Cambridge University Press



(a) X-section of both zones (b) Y-section of both zones

Fig. 1 Slice meshes of both zones.



(a) Overlapping grid of gap between the bottom of the hub and the fairing (b) Grid near the overlapping boundary

Fig. 2 Partially enlarged view of the slice mesh.

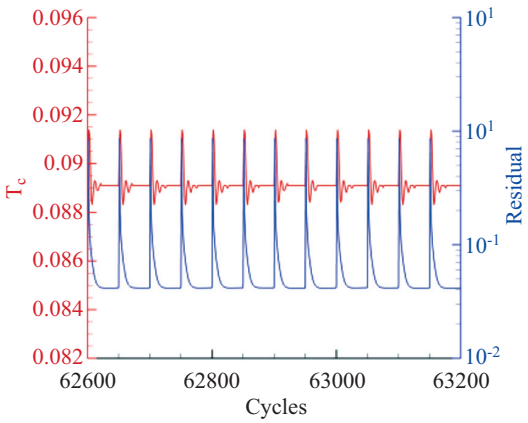


Fig. 3 Convergence history of sub-iteration and thrust coefficient.

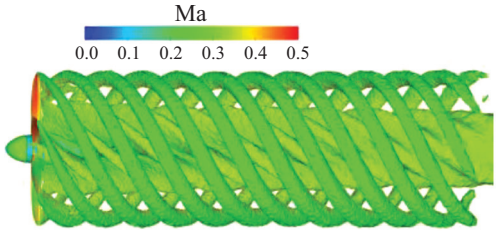


Fig. 4 Iso-surface of the Q-criterion colored by Mach number.

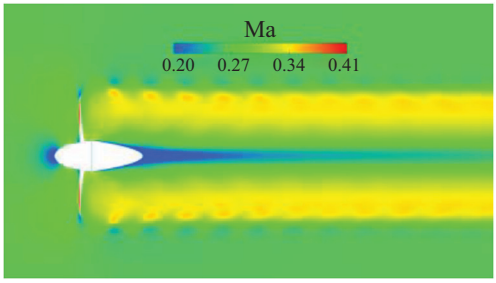
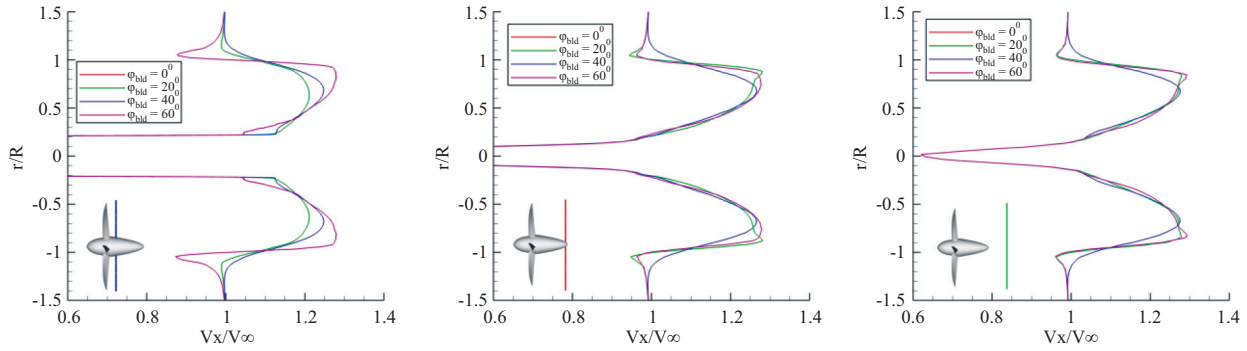


Fig. 5 Mach number contours of Y = 0m section.

interpolated boundary surface. In order to eliminate the problem of large meshless area around the gap caused by hole-cutting, the surface mesh size is controlled at the bottom of the hub and the front end of the fairing, as shown in Fig. 2(a). Figure 2(b) shows the spatial grid near the interpolation boundary. It can be seen that the mesh size in the interpolated boundary of the two zones is matched. From the interpolated boundary surface to the space, there are triangular prisms, pyramids and tetrahedral meshes.

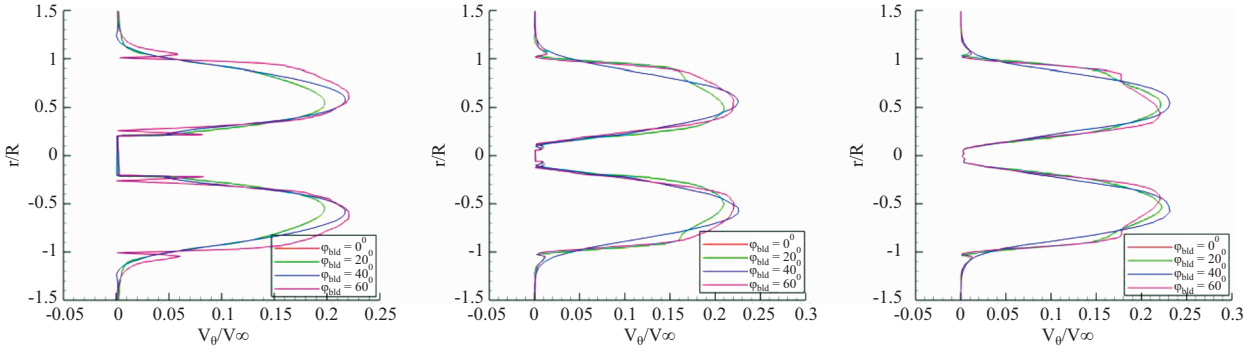
Figure 3 shows the sub-iteration residual convergence history and the thrust coefficient convergence history when the advance ratio is 1.292, red line is the thrust coefficient curve, and blue line is the sub-iterative residual convergence curve. The thrust coefficient of propeller is defined as $Tc = T \Big/ \frac{1}{2}\rho v^2 s$, where, the T is the thrust of propeller, ρ is the density of air, v is the velocity of freestream, and s represents the propeller area. The number of sub-iteration steps is 50, and residuals of sub-iterations converge quickly after reduction of more than one order of magnitude due to multi-grid method and local time-stepping. Figure 4 shows the iso-surface of the Q-criterion colored by Mach number. The space vortex caused by rotation of the propeller can be clearly observed because meshes behind the propeller are refined and the blade profile leads to the trailing edge vortex. Figure 5 shows the Mach number contours of Y

https://doi.org/10.1017/jmech.2017.50 Published online by Cambridge University Press



(a) x/R = 0.11 (b) x/R = 0.658 (c) x/R = 1.146

Fig. 6 Ratio of axial velocity to incoming velocity of three different axial positions at different azimuth angles.



(a) x/R = 0.11 (b) x/R = 0.658 (c) x/R = 1.146

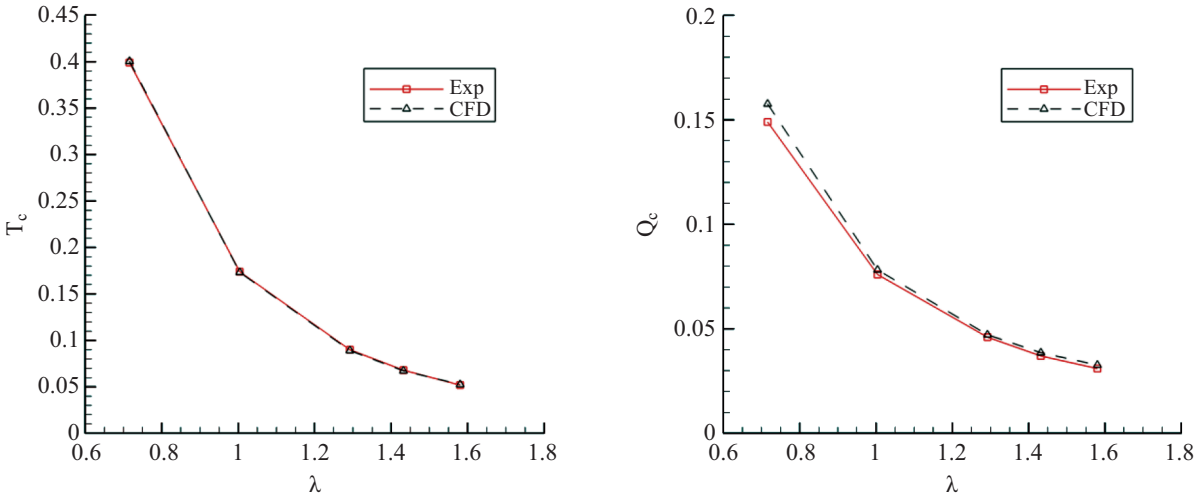
Fig. 7 Ratio of tangential velocity to incoming velocity of three different axial positions at different blade azimuth angles.

= 0m section, and there is a strongly unsteady flow in the slipstream area due to the tip vortex. In Fig. 5, the Mach number contours of the two overlapping regions is continuous and smooth, further validating the overlapping method and the grid technology. The acceleration effect and the swirl effect of the propeller slipstream can be seen from the Mach number contours. With the slipstream developing to downstream, flow tube cross-sectional area continues to shrink slowly.

In order to describe the results, the azimuthal positions relative to axis of propeller rotation are used. φ = 0° is defined at the top of the nacelle and increases in the direction of propeller rotation. Figure 6 shows the velocity profiles of three different axial positions at different blade azimuth angles, where the abscissa gives the ratio of the axial velocity to the incoming flow velocity, and the ordinate is the ratio of the distance to radius. The axial positions are marked with blue, red, green lines in Figs. 6(a), (b) and (c), and the position of x/R are 0.110, 0.658, 1.146. The azimuth angle of three axial cross section is 90 degrees. Because the propeller has six blades, with a period of 60°, so velocity distribution is periodical at every 60° azimuth. In Figs. 6(a), (b) and (c), the propeller accelerates the airflow behind and leads to the blade tip vortex, the axial velocity extremum appears near the propeller tip. From the three graphs, the closer the section is to the propeller, the more unsteady the effect is, and the greater difference in the cross-section velocity of different blade azimuth angles becomes. Figure 7 shows the tangential velocity distribution of three different axial positions at different blade azimuth angles, where the abscissa gives the ratio of tangential velocity to the incoming velocity. In Figs. 7(a), (b) and (c), the propeller rotates the airflow behind. The closer the section is to the propeller, the greater the difference is in the cross-section tangential velocity of different azimuth angles. The tangential velocity extremum appears near the middle of the blade. From actuator disk model, the tangential velocity behind the disk is defined as $V_\theta = V_\theta' + \Delta V_\theta = (V_y \cos\varphi - V_z \sin\varphi) + \frac{NW^2 c}{4\pi r V_x}(C_L \sin(\alpha_i) + C_D \cos(\alpha_i))$, where V_x, V_y, V_z, N, W, c, α_i, C_L, C_D denote the velocity before blades in the Cartesian coordinate system, number of blades, synthetic velocity, chord length, induced angle of attack, lift coefficient, and drag coefficient of airfoil, respectively. From the formula, the tangential velocity is related to radius, lift coefficient, drag coefficient and induced angle of attack. C_L/C_D and α_i are small at the tip of the blades, so the tangential velocity doesn't appear at the tip of the blade.

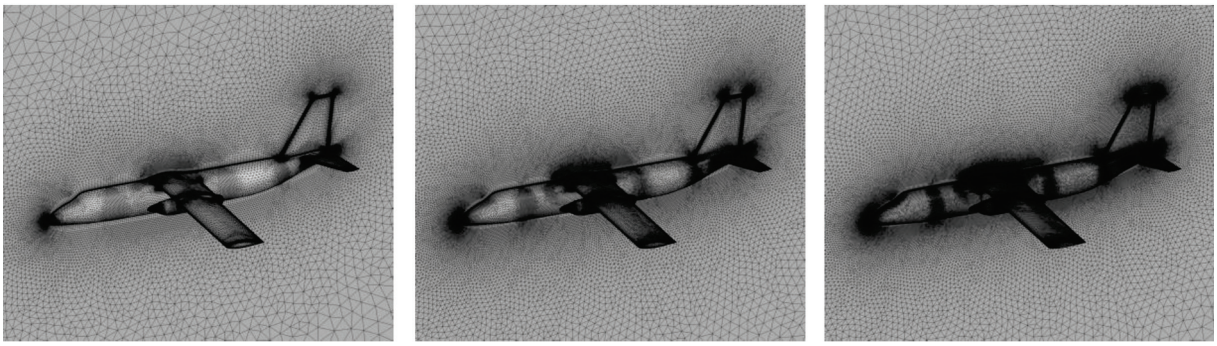
Figure 8 shows a comparison of the experimental and calculated propeller thrust coefficient and torque coeffi-

https://doi.org/10.1017/jmech.2017.50 Published online by Cambridge University Press



(a) Comparison of the thrust coefficient (b) Comparison of the torque coefficient

Fig. 8 Isolated-propeller dynamic characteristics.



(a) Coarse (b) Medium (c) Fine

Fig. 9 Surface and symmetry grid of steady-state configuration with no propeller.

cient, where the abscissa is the propeller advance ratio. The numerical results show a good agreement with the experimental data, thus verifying the simulation method for propeller slipstream.

3.2 Effect of Propeller Slipstream on Aircraft

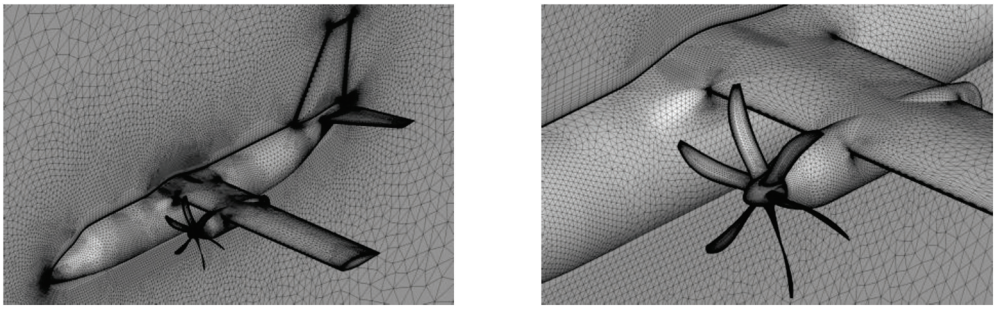
Numerical simulation of the propeller slipstream is a turboprops model. The installation angle of wing and the propeller are 3° and 1°, respectively. The propeller rotates with the speed of 1050 rpm and counterclockwise when looking from the front. The freestream condition are as follows: $\mathrm{Re}_u = 4.14 \times 10^6$, $Ma = 0.316$, $T_\infty = 249.2$. The angles of attack in computation ranges from 2°~10°. The unsteady inner iteration is 100 steps and the propeller rotates by 2° per real physical time step. Only a half fuselage is simulated in order to save the number of grid cell. To compare the effects of slipstream, two configurations are simulated, one for the steady-state configuration with no propeller and the other for the unsteady-simulated configuration with propeller. First, grid independent study is carried out to verify the numerical solutions. Figure 9 shows the surface and symmetry plane grid of three grid levels. The number of grid cells used for steady calculation is 3.77 million, 9.19 million and 18.29 million. The number of grid cells in aircraft major-zone for unsteady computation is 12.13 million, 17.34 million, 25.55 million, and the number of grid cells in propeller subzone for unsteady computation is 4.19 million, 8.35 million, 12.57 million. The force and moment prediction of different grids at an angle of attack of $\alpha = 4°$ are presented in Table 2, where the slipstream results is a time average over one period. As shown in the table, the effect of slipstream on aircraft at three grid levels is consistent. Slipstream decreases the lift coefficient and the yaw moment coefficient while increasing the drag coefficient, the pitching moment coefficient and the roll moment coefficient. It is appropriate to use the coarse grid to study the effect of propeller slipstream at different angles of attack.

Figure 10 shows the surface and symmetry plane grid of turboprops. The anisotropic triangular mesh is used in the leading edge and trailing edge of wing, and similar mesh is used on the blades. Figure 11 shows the overlapping slice meshes of engine symmetry, where red indicates the propeller grid and blue denotes the aircraft

https://doi.org/10.1017/jmech.2017.50 Published online by Cambridge University Press

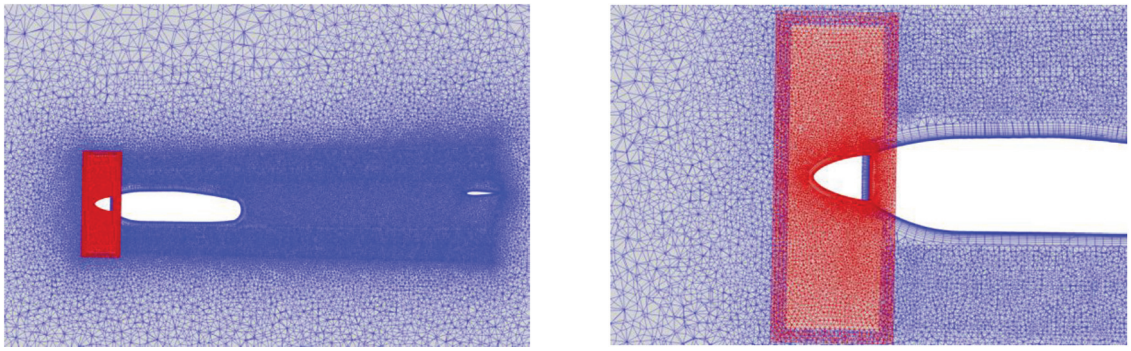
Table 2 Numerical results of different grids

Grid label	Coarse			Medium			Fine		
	Steady	Slipstream	Difference	Steady	Slipstream	Difference	Steady	Slipstream	Difference
C_L	0.3449	0.3387	-0.0062	0.3428	0.3378	-0.0050	0.3444	0.3399	-0.0045
C_D	0.0242	0.0265	0.0023	0.0238	0.0262	0.0024	0.0230	0.0259	0.0029
C_n	0.0090	0.0081	-0.0009	0.0091	0.0082	-0.0009	0.0091	0.0082	-0.0010
C_m	-0.0049	0.0304	0.0354	-0.0045	0.0329	0.0373	-0.0046	0.336	0.0382
C_l	0.0626	0.0639	0.0013	0.0624	0.0636	0.0013	0.0627	0.0641	0.0014



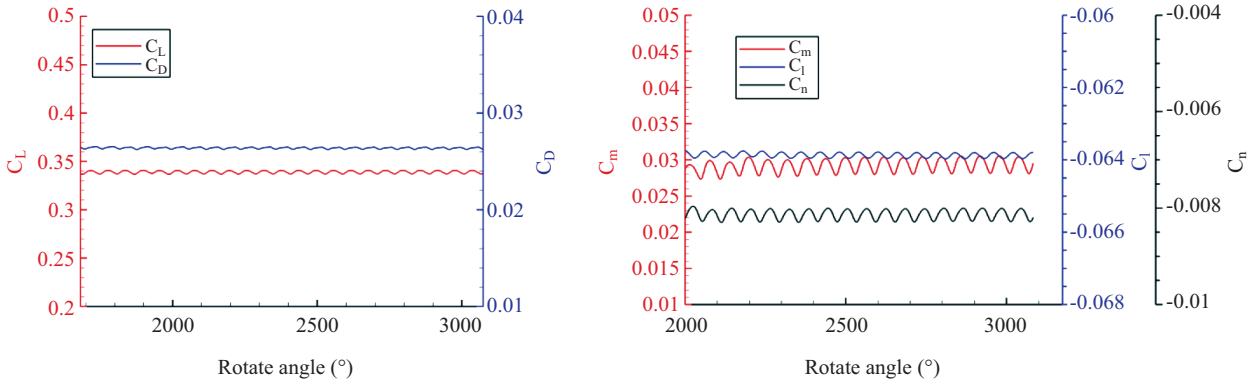
(a) Surface and symmetry mesh (b) Propeller and wing surface mesh enlargement

Fig. 10 Surface and symmetry grid of turboprops.



(a) Slice mesh of engine symmetry (b) Slice mesh enlargement

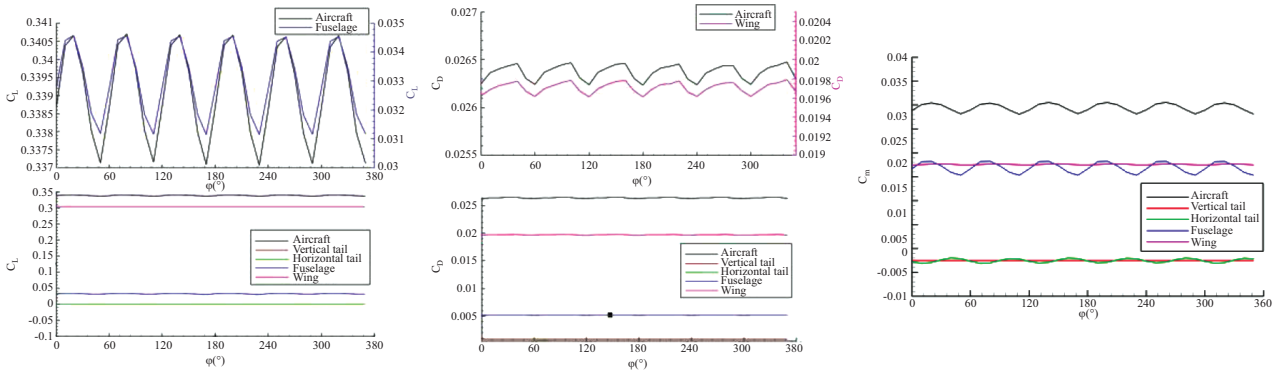
Fig. 11 Slice mesh of both subzones.



(a) Convergence of lift drag coefficient (b) Convergence of moment coefficient

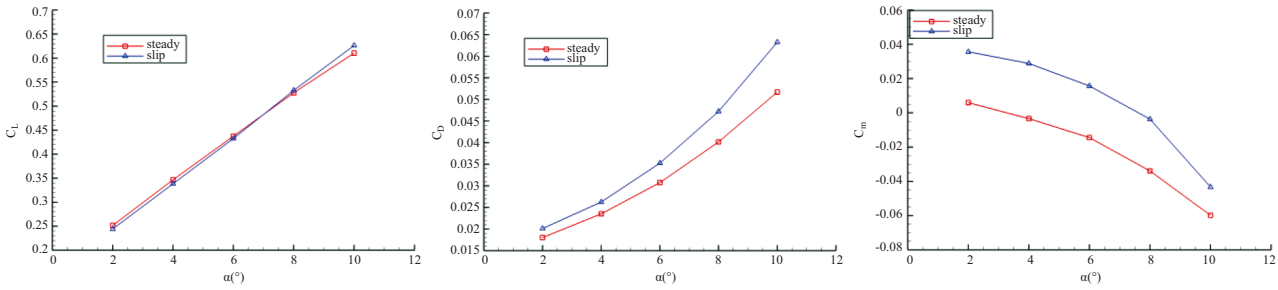
Fig. 12 Convergence of aerodynamic force.

https://doi.org/10.1017/jmech.2017.50 Published online by Cambridge University Press



(a) Lift coefficient breakdown (b) Drag coefficient breakdown (c) Pitching moment coefficient breakdown

Fig. 13 Propeller slipstream effect on components of aircraft.



(a) Lift coefficient (b) Drag coefficient (c) Pitching moment coefficient

Fig. 14 Comparison of the aerodynamic characteristics of turboprops.

grid. In order to accurately simulate the effect of slipstream, the isotropic tetrahedral meshes of the same scale are used to refine the space grid behind the propeller, and the entire refinement area extends to the trailing edge of the flat tail. Figure 10(b) is a magnified view of the overlapped grid, showing the mesh near the gap between stationary and rotating parts and the overlapping area of two grids. In addition to the gap, other overlapping regions are tetrahedral mesh of the same scale, and meanwhile ensure three or four rows of interpolation grids in the overlapping regions.

Figure 12 shows the convergence of aerodynamic force at $\alpha = 4°$. The abscissa in the figure is the rotation angle of the propeller. It can be seen that, due to the long fuselage, the propeller needs to rotate almost seven cycles to fully establish the stable periodic slipstream field. The lift, drag and torque coefficients of the aircraft exhibit periodically oscillation with a period of 60°. This fluctuation can be attributed to the mutual interaction between the propeller and aircraft, which leads to aircraft being affected by an altered flowfield as blade passes in front of the wing on its downward and upward rotation. Figure 13 shows the breakdown of the lift, drag and pitching moment coefficients on aircraft; the impact of slipstream on components of aircraft can be clearly seen. As the fuselage is on the side of the propeller, the lift coefficient oscillation is mainly reflected on the fuselage. Because the wing is closest to the propeller, the drag coefficient oscillation is mainly reflected on the wing. Since the horizontal tail is far from the moment reference point, and a smaller lift oscillation can lead to a larger pitch moment, the pitching moment coefficient oscillation is mainly reflected on the fuselage and horizontal tail.

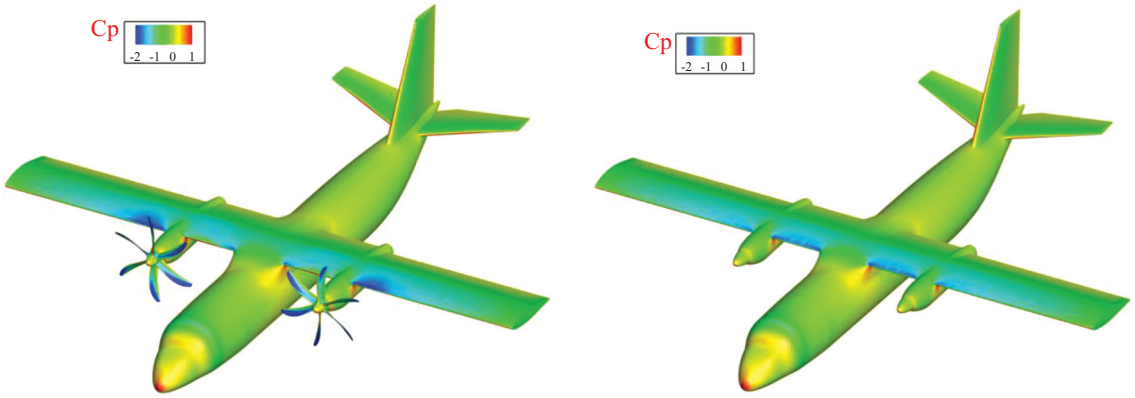
Figure 14 shows the aerodynamic characteristics of aircraft with the angle of attack. The results are compared with those steady flow without propeller, the red line is steady flow, the blue line is unsteady slipstream which is a time average over one period. It can be seen that the slipstream increases the slope of the lift coefficient, and increases the drag coefficient and the nose up pitching moment significantly. The propeller injects energy by rotation and the slipstream accelerates the flow behind the propeller, which is equivalent to increasing the local Mach number of airflow on wing. The increase in Mach number leads to an increase in the slope of lift coefficient and drag coefficient.

In order to analyze the effect of slipstream on the airplane components, Table 3 gives the lift coefficient of aircraft components at an angle of attack of 4 °; it can be seen that the slipstream causes a slight increase in the lift coefficient of wing, a significant reduction in the lift coefficient of horizontal tail, and a reduction in the lift coefficient of fuselage. The joint action of the downwash of wing and the slipstream causes the lift coefficient on the horizontal tail to decrease. The decrease of the horizontal tail lift force leads to a significant increase of pitching moment. Because the propeller rotates coun-

https://doi.org/10.1017/jmech.2017.50 Published online by Cambridge University Press

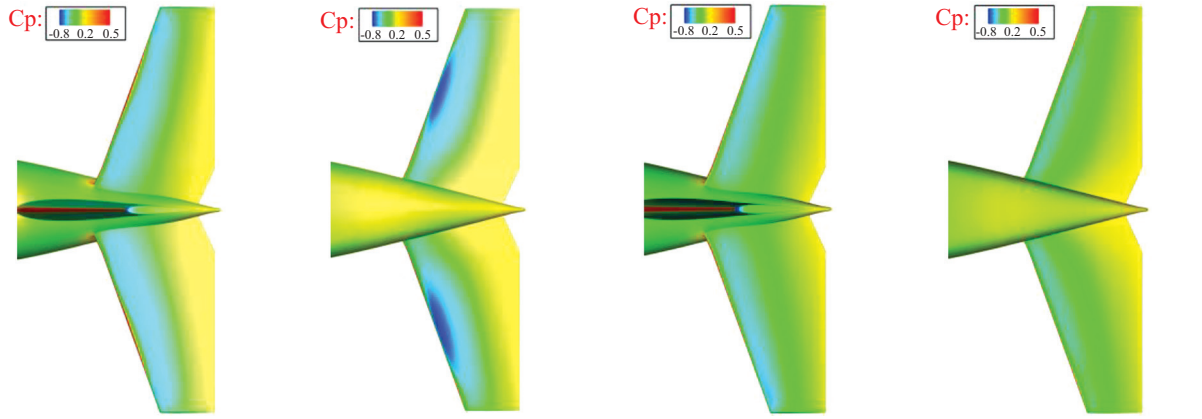
Table 3 Comparison of lift coefficient of aircraft components at an angle of attack of 4°.

	Wing	Horizontal tail	Vertical tail	Fuselage
Slipstream	0.29759	0.00048	0.00067	0.03302
Steady flow	0.29279	0.00728	0.00068	0.03469



(a) Slipstream (b) Steady flow

Fig. 15 Surface pressure distributions.



(a) Slipstream (upper surface) (b) Slipstream (lower surface) (c) steady flow (upper surface) (d) steady flow (lower surface)

Fig. 16 Horizontal tail pressure contours.

terclockwise when looking from the front, resulting in reduced local angle of attack of fuselage, the lift coefficient decreases.

Figure 15 shows the pressure distributions of aircraft with or without slipstream. The pressure contour is symmetrically processed. As can be seen from the figure, the slipstream affects the wing pressure distribution, especially the wing sections behind the propeller. On the side of the nacelle with an upward rotation of the blades a locally positive angle of attack is the result, leading to a positive lift force being produced by wing, while on the other side of nacelle the situation is reversed. Figure 16 shows the surface pressure distribution of horizontal tail. Due to the downwash effect of the slipstream and wing, the pressure at the lower surface of horizontal tail is reduced, resulting in a decrease of the lift force and an increase of the pitching moment.

To further analyze the influence of slipstream, the pressure distributions of the wing sections and the horizontal tail sections are provided. Figure 17 shows the profile positions. In Fig. 18, the surface pressure coefficients distribution for different profiles of the left wing

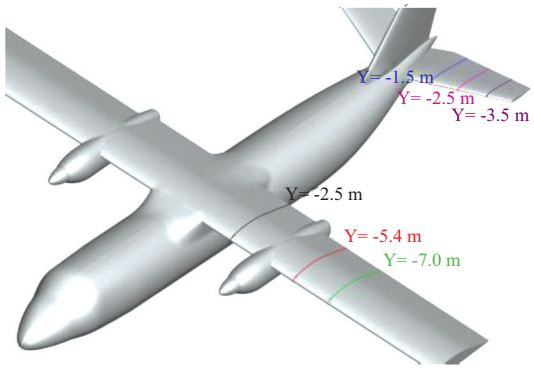
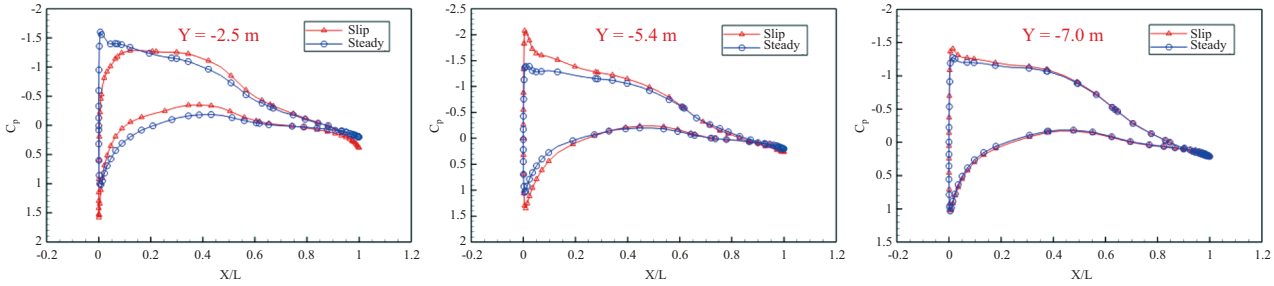


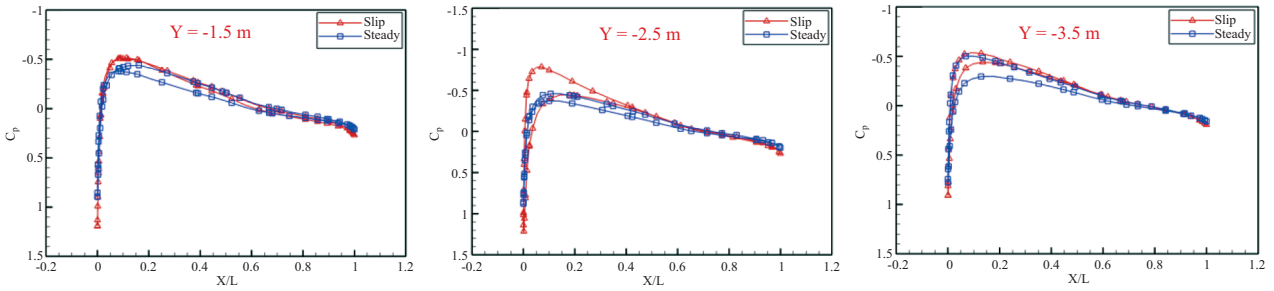
Fig.17 Different sections on wing and horizontal tail.

https://doi.org/10.1017/jmech.2017.50 Published online by Cambridge University Press



(a) Pressure profiles at y = -2.5 m (b) Pressure profiles at y = -5.4 m (c) Pressure profiles at y = -7.0m

Fig. 18 Pressure distributions on different sections of wing.



(a) Pressure profiles at y = -1.5 m (b) Pressure profiles at y = -2.5 m (c) Pressure profiles at y = -3.5 m

Fig. 19 Pressure distributions on different sections of horizontal tail.

are presented, and the steady surface pressure distribution for the same sections are also presented to compare with the unsteady results. The red line is unsteady slipstream, and the blue line is steady flow. It can be seen that slipstream has a significant influence on the pressure profile of wing sections. As shown in Fig. 18(a), the section is located on the side of the nacelle with a downward rotation of the blades, the leading edge suction peak disappears on the upper surface of the section and the suction peak appears at the leading edge of the lower surface, and then the lift coefficient decreases. Lift coefficient of the section shown in Figs. 18(b), (c) increase due to the increase of local angle of attack. The closer the profile is to the propeller, the greater the influence is.

Figure 19 shows the distribution of pressure profiles at different horizontal tail sections. Again results from the slipstream and steady flow are shown in red and blue lines respectively. As is shown, the horizontal tail is in the region of slipstream, and the pressure distribution on the horizontal tail surface changes greatly.

Figure 20 shows the iso-surface of the Q-criterion colored by Mach number. Because the space grid behind the propeller is refined by isotropic tetrahedral mesh, as can be seen in Fig. 11, the numerical dissipation is reduced. Due to the small numerical dissipation, the vortices can be clearly observed within a long distance. The presence of wing destroys the continuity of the blade tip vortices. Figures 21 and 22 show the vorticity contours at the sections of x = 11 m and y = -3.95 m. The propeller rotation is prescribed to be perfectly synchronized with blade passage in phase. The presence of

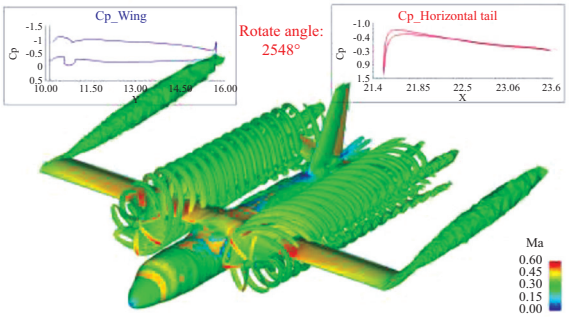


Fig. 20 Iso-surfaces of the Q-criterion colored by Mach number.

wing hinders the rotation of slipstream, which causes the blade tip vortices on the upper and lower wing surfaces to stagger in streamwise and spanwise location. The shrinkage of slipstream can be seen in Fig. 22. It can be seen that the horizontal tail is completely in the propeller slipstream, causing the pitching moment to change greatly, as shown in Table 3.

Figure 23 shows the Mach number contours at the section of Y = -2.5 m. Duo to rotation, the propeller accelerates the airflow behind it, especially the airflow on the upper and lower surfaces of wing. Mach number of airflow on the upper and lower surfaces of wing is obviously increased, causing the slope of lift coefficient to increase, as can be seen in Fig. 14(a). Figure 24 shows the pressure distribution and streamline at the section of Y = -2.5 m. From the streamline, the downwash

https://doi.org/10.1017/jmech.2017.50 Published online by Cambridge University Press

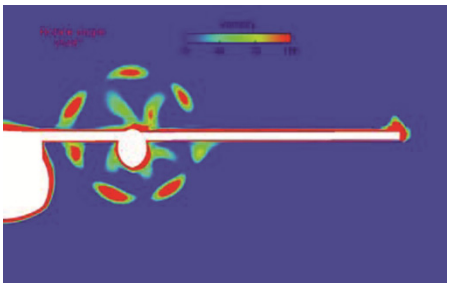


Fig. 21 Vorticity contours at x = 11m.

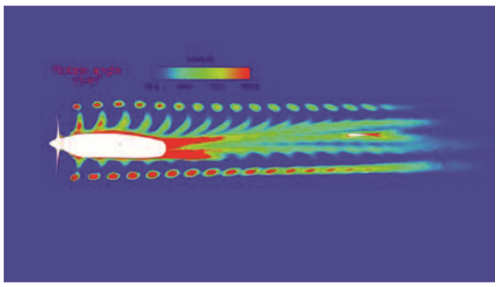
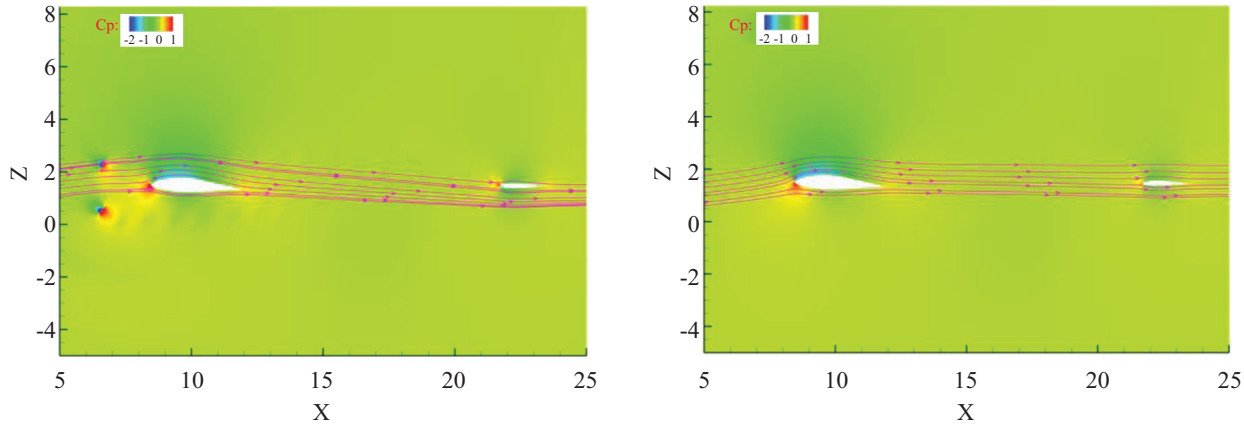


Fig. 22 Vorticity contours at y = -3.95m



(a) Slipstream (b) Steady

Fig. 23 Mach number contours at y = -2.5m.



(a) Slipstream (b) Steady

Fig. 24 Streamline profile at y = -2.5m.

of slipstream is shown clearly, which is mainly from two aspects, one is from the increase of lift on wing, which causes a stronger downwash, and the other is from the slipstream of propeller.

4. CONCLUSIONS

Based on the anisotropic unstructured hybrid grid, and in combination with the dynamic overlapping grid, the unsteady propeller slipstream around the isolated-propeller and turboprops are numerically simulated by solving URANS equations. A comparison with propeller slipstream data obtained in the CARDC wind tunnel has been performed and the numerical results show good agreement with the experimental data, thus verifying the simulation method and grid technology. The effect of slipstream is analyzed by the instantaneous axial and tangential velocity of different axial stations behind the propeller under different blade azimuth angles. The numerical results show the very pronounced unsteady effects present in the slipstream, and the tangential velocity behind propeller is not only related to the radius, but also to the lift coefficient, drag coefficient and induced angle of attack. The lift-drag ratio and the induced angle of attack at the tip of blade are small, resulting in the maximum tangential velocity does not appearing at the tip.

https://doi.org/10.1017/jmech.2017.50 Published online by Cambridge University Press

An analysis of the complex mutual aerodynamic interactions between the propeller and aircraft has been presented for turboprop. Grid independent study is carried out to establish the numerical results, and the effect of slipstream on aircraft at three grid levels is consistent. The aerodynamic characteristics of the aircraft with/without slipstream are given, and slipstream increases drag coefficient, pitching moment coefficient and the slope of lift coefficient. Because slipstream increases the local Mach number of airflow on wing, causing the slope of aircraft's lift curve and the lift coefficient on wing to increase. Under the combined action of the downwash of wing and the slipstream, the local angle of attack of horizontal tail decreases and the lift coefficient on the horizontal tail decreases, resulting in a large rise in pitching moment. Because of the mutual interaction between the propeller and aircraft, the lift, drag and torque coefficients of aircraft exhibit periodically oscillation. The presence of wing hinders the rotation of slipstream and destroys the continuity of the blade tip vortices, causing the blade tip vortices on the upper and lower wing surfaces to stagger in streamwise and spanwise location.

NOMENCLATURE

C_L Lift coefficient, $C_L = L \Big/ \frac{1}{2}\rho V_\infty{}^2 s$;

C_D Drag coefficient, $C_D = D \Big/ \frac{1}{2}\rho V_\infty^2 s$;

C_m Pitching moment coefficient, $C_m = M \Big/ \frac{1}{2}\rho V_\infty^2 sc$;

C_n Yawing moment coefficient, $C_n = N \Big/ \frac{1}{2}\rho V_\infty^2 sb$;

C_l Rolling moment coefficient, $C_l = l \Big/ \frac{1}{2}\rho V_\infty^2 sb$;

T_c Thrust coefficient, $Tc = T \Big/ \frac{1}{2}\rho V_\infty^2 s$;

Ma Mach number;

ω Rotation angular velocity, *rad/s*;

V_x, V_y, V_z The flow velocity in Cartesian coordinate system, *m*/*s*;

V_∞ The incoming flow velocity, *m*/*s*;

V_θ The tangential velocity, $V_\theta = (V_y\cos\varphi - V_z\sin\varphi) + \frac{NW^2 c}{4\pi r V_x}(C_L \sin(\alpha_i) + C_D \cos(\alpha_i))$, *m*/*s*;

α_i Induced attack angle, $\alpha_i = \arctan\left(\frac{V_x}{\omega r - V_\theta'}\right)$, °;

W The synthetic velocity, $W = \sqrt{V_x^2 + (\omega r - V_\theta')^2}$, *m*/*s*;

C_p Pressure coefficient, $C_p = (p - p_0) \Big/ \frac{1}{2}\rho v^2$;

λ Propeller forward ratio, $\lambda = V/n_s D$;

ρ Density, kg/m^3;

s Reference area, m^3;

b Reference span length, *m*;

c Reference chord length, *m*;

φ Azimuth angle, °;

φ_{bld} Blade azimuthal position, °;

r Radial position, *m*;

N Number of blades;

x The axil distance from the rear of hub, *m*;

Re_u Unit Reynolds number.

REFERENCES

1. Hunsaker, D. and Snyder, D., "A Lifting-Line Approach to Estimating Propeller/Wing Interactions," *24th Applied Aerodynamics Conference*, San Francisco, USA (2006).
2. Landahl, M. T. and Stark, V. J. E., "Numerical Lifting -Surface Theory — Problems and Progress," *AIAA Journal*, **6**, pp. 2049-2060 (1968).
3. Conway, J. T., "Analytical Solutions for The Actuator Disk with Variable Radial Distribution of Load," *Journal of Fluid Mechanics*, **297**, pp. 327-355 (1995).
4. Conway, J. T., "Exact Actuator Disk Solutions for Nonuniform Heavy Loading and Slipstream Contraction," *Journal of Fluid Mechanics*, **365**, pp. 235-267 (1998).
5. Nam, H. J., Park, Y. M. and Kwon, O. J., "Simulation of Unsteady Rotor-Fuselage Aerodynamic Interaction Using Unstructured Adaptive Meshes," *Journal of the American Helicopter Society*, **51**, pp. 141-149 (2006).
6. Stuermer, A. W., "Unsteady CFD Simulations of Propeller Installation Effects," *42nd AIAA/ASME/SAE/ASEE Joint Propulsion Conference & Exhibit*, California, USA (2006).
7. Roosenboom, E. W. M., Sturmer, A. and Schroder, A., "Advanced Experimental and Numerical Validation and Analysis of Propeller Slipstream Flows," *Journal of Aircraft*, **47**, pp. 284-291 (2010).
8. Xu, H. Y. and YE, Z. Y., "Numerical Study of Propeller Slipstream Based on Unstructured Overset Grids," *Journal of Aircraft*, **49**, pp. 384-389 (2012).
9. Spalart, P. R. and Allmaras, S. R., "A One-Equation Turbulence Model for Aerodynamic Flows," *30th Aerospace Sciences Meeting & Exihibit*, Reno, USA (1992).
10. Jameson, A., "Time Dependent Calculations Using Multi-Grid, with Applications to Unsteady Flows Past Airfoils and Wings," *10th Computational Fluid*

https://doi.org/10.1017/jmech.2017.50 Published online by Cambridge University Press

Dynamics Conference, Honolulu, USA (1991).

11. Yoon, S. and Jameson, A., "Lower-Upper Implicit Schemes with Multiple Grids for the Euler Equations". *AIAA Journal*, **26**, pp.1025-1026 (1988).
12. Blazek, J., *Computational Fluid Dynamics: Principles and Applications*, First Edition, Elsevier Science Ltd, Oxford, pp. 305-319 (2001).
13. Chen, J. T., Zhang, Y. B., Zhou, N. CH. and Deng, Y. Q., "Numerical Investigations of the High-Lift Configuration with MFlow Solver," *Journal of Aircraft*, 52, pp. 1051-1062 (2015).
14. Gong, X. Q., Chen, J. T., Zhou, N. CH., Zhang, Y. B. and Deng, Y. Q., "The Effects of Turbulence Model Corrections on Drag Prediction of NASA Common Research Model," *32nd AIAA Applied Aerodynamics Conference*, Atlanta, USA (2014).
15. David W. L. *et al.*, "Summary of Data from the Fifth AIAA CFD Drag Prediction Workshop," *51st AIAA Aerospace Sciences Meeting including the New Horizons Forum and Aerospace Exposition, Aerospace Sciences Meetings*, Texas, USA (2013).
16. https://aiaa-dpw.larc.nasa.gov (2016).
17. Roe, P. L., "Approximate Riemann Solvers, Paremeter Vectors, and Difference Schemes," *Journal of Computational Physics*, 143, pp. 125-158 (1981).
18. Venkatakrishnan, V., "On the Accuracy of Limiters and Convergence to Steady State Solutions," *31st Aerospace Sciences Meeting & Exihibit*, Reno, USA (1993).
19. Bonet, J., "An Alternating Digital Tree (ADT) Algorithm for 3D Geometric Searching and Intersection Problems," *International Journal for Numerical Methods in Engineering*, **31**, pp. 1-17 (1991).

(Manuscript received December 11, 2016,
accepted for publication June 8, 2017.)

https://doi.org/10.1017/jmech.2017.50 Published online by Cambridge University Press